IOPscience iopscience.iop.org

Home Search Collections Journals About Contact us My IOPscience

Central safety factor and $_N$ control on NSTX-U via beam power and plasma boundary shape modification, using TRANSP for closed loop simulations

This content has been downloaded from IOPscience. Please scroll down to see the full text.

View the table of contents for this issue, or go to the journal homepage for more

Download details:

IP Address: 198.125.233.17
This content was downloaded on 13/07/2015 at 15:56

Please note that terms and conditions apply.

IOP Publishing | International Atomic Energy Agency Nuclear Fusion
Nucl. Fusion **55** (2015) 053033 (15pp) doi:10.1088/0029-5515/55/5/053033

Central safety factor and β_N control on NSTX-U via beam power and plasma boundary shape modification, using TRANSP for closed loop simulations

M.D. Boyer[1], R. Andre[1], D.A. Gates[1], S. Gerhardt[1], I.R. Goumiri[2] and J. Menard[1]

[1] Princeton Plasma Physics Laboratory, Princeton, NJ 08544, USA
[2] Department of Mechanical and Aerospace Engineering, Princeton University, Princeton, NJ 08544, USA

E-mail: mboyer@pppl.gov

Received 8 November 2014, revised 9 March 2015
Accepted for publication 17 March 2015
Published 23 April 2015

Abstract

The high-performance operational goals of NSTX-U will require development of advanced feedback control algorithms, including control of β_N and the safety factor profile. In this work, a novel approach to simultaneously controlling β_N and the value of the safety factor on the magnetic axis, q_0, through manipulation of the plasma boundary shape and total beam power, is proposed. Simulations of the proposed scheme show promising results and motivate future experimental implementation and eventual integration into a more complex current profile control scheme planned to include actuation of individual beam powers, density, and loop voltage. As part of this work, a flexible framework for closed loop simulations within the high-fidelity code TRANSP was developed. The framework, used here to identify control-design-oriented models and to tune and test the proposed controller, exploits many of the predictive capabilities of TRANSP and provides a means for performing control calculations based on user-supplied data (controller matrices, target waveforms, etc). The flexible framework should enable high-fidelity testing of a variety of control algorithms, thereby reducing the amount of expensive experimental time needed to implement new control algorithms on NSTX-U and other devices.

Keywords: spherical torus plasma control, current profile control, optimal control, control-oriented modelling

(Some figures may appear in colour only in the online journal)

1. Introduction

The national spherical torus experiment upgrade facility (NSTX-U) [1], has been designed to bridge the gap between present ST devices, like NSTX [2] or the mega-ampere spherical tokamak (MAST) [3], and the requirements of future facilities that will study plasma material interaction [4], nuclear components [5], and generation of fusion power [6]. NSTX-U aims to improve understanding of key issues, such as the scaling of electron transport with field and current [7–10], fast particle physics [11–14], and sustainment of non-inductive, high-β scenarios [15–20]. The primary components of the upgrade are the complete replacement of the 'centre stack', (containing the inner-leg of the toroidal field (TF) coils, the Ohmic heating (OH) solenoid, and some divertor coils), and the addition of a second neutral beam injector, aimed more tangentially. The upgrade will increase the TF capability from 0.55 to 1.0 T, the maximum plasma current from 1.3 to 2.0 MA, and significantly increase auxiliary heating power, neutral beam current drive (NBCD), and the ability to tailor their deposition profiles.

In order to achieve the goals of the NSTX-U program, advancements in plasma control will be essential, and work is underway to upgrade the hardware and software of the plasma control system (PCS) [21], and to develop the new control algorithms needed to optimally handle the complex dynamics of the system. The development of algorithms for plasma boundary shape control, power and particles exhaust control, current and rotation profiles control, and edge transport barrier control is in progress, and these efforts will build on the successful advances made on NSTX [22–26].

Due to its effect on confinement, plasma stability, and non-inductively driven plasma current, control of the safety factor profile will be critical to the NSTX-U program goals.

 Not subject to copyright in the USA/Contribution of the Department of Energy Printed in the UK

Feedback control of the safety factor profile on NSTX-U will be made possible through the use of motional Stark effect (MSE) magnetic field pitch angle measurements [27] as constraints in the real-time equilibrium reconstruction code rtEFIT [22, 28]. Much progress in controlling the current profile has recently been made on several machines, including DIII-D, JET, and JT-60U, especially in the area of model-based feedback control. By combining the poloidal magnetic flux diffusion equation with empirical correlations obtained from physical observations and experimental data from DIII-D for the electron temperature, plasma resistivity, and non-inductive current drive, a simplified nonlinear model describing the dynamic response of the current profile to induction, the auxiliary heating and current drive systems, and the line average density in L-mode discharges was obtained [29]. The control-oriented model was used to design feedback controllers using robust [30], optimal [31], and backstepping [32] control design approaches, and the feedback controllers were successfully tested in experiments in DIII-D. A similar approach is currently being developed for NSTX-U. Using an alternative, purely data-driven approach to modelling, scenario-specific linear, dynamic, response models were recently obtained in JET [33], JT-60U, and DIII-D [34], which were used to design controllers for simultaneous control magnetic and kinetic plasma profiles.

In most studies of safety factor profile control, the plasma boundary shape is controlled (by a separate existing controller) at some constant reference, and the magnetic geometry is assumed to be fixed in time in the control design. However, modulation of the plasma shape has important effects on the bootstrap current, beam driven current deposition profiles, and magnetic flux diffusion, and therefore, the safety factor profile. Thus, plasma shape could serve as an additional degree of freedom in controller designs. While there are many shaping parameters that could be modified, there are several goals and constraints to consider when choosing a plasma boundary shape. On NSTX-U it is desirable to keep the inner plasma wall gap small to maintain low aspect ratio and best utilization of the TF. The upper and lower gaps should be kept small to achieve high elongation, and high plasma triangularity is needed to improve TF utilization. This leaves the outer-midplane plasma-wall gap as a free parameter to manipulate for the purposes of safety factor profile control (though not considered in this work, the plasma 'squareness' could potentially be manipulated, provided the device has sufficient shaping flexibility [35, 36]). The outer-gap size is a trade-off, as a smaller outer-gap causes the plasma to fully fill the vessel, while a large outer gap increases elongation, and therefore bootstrap current. Increasing the outer gap size also causes the off-axis beams to drive current further off-axis. In [37], this trade-off was explored by generating a series of target plasma boundary shapes with identical X-point and inner-midplane radii, and identical X-point heights. Outer-gap sizes in the range of 5 to 20 cm were considered, with a corresponding range of elongation from 2.55 to 2.95 and aspect ratio from 1.71 to 1.81. It was observed that increasing the outer-gap size increased the central safety factor (and $q_{\min}$), which is critical for avoiding non-resonant $m/n = 1/1$ kink modes [20, 38–41], which are often coupled to 2/1 islands, on NSTX-U [42]. It was also seen that shine-through power becomes significant for large outer-gap, while the bad-orbit loss becomes significant for small outer-gap. The ideal-wall stability limit, resistive wall mode (RWM) stability, and vertical controllability will also depend on outer gap through varied coupling to the passive plates and elongation. The influence of the outer-gap on plasma parameters, combined with uncertainty in modelling, motivates the use of a feedback control system to alter the outer-gap size in response to real-time measurements of plasma performance.

In this work, we consider the controlled manipulation of the outer-midplane plasma-wall gap, along with the total beam power, as a potential means for controlling the central safety factor and β_N in NSTX-U. While this work focuses on just two actuators, the approach could later be integrated into a more complex profile control scheme that simultaneously modulates outer-gap size, beam power distribution, density, and loop voltage, providing an additional degree of freedom for achieving current profile targets. Two control design approaches were used, each using reduced models of the system dynamics. Since experimental data is not yet available for NSTX-U, these models were identified from simulated data generated using predictive TRANSP simulations (the proposed methods for identification can later be applied to experimental data). TRANSP, a time dependent code developed at Princeton Plasma Physics Laboratory for both prediction and analysis of tokamak experimental data [43–45], is one of the primary codes used in the fusion community. Several widely used modules, including NUBEAM [46] for calculating neutral beam heating and current drive and the ISOLVER free-boundary equilibrium solver [47, 48], are available for use within TRANSP and make it well suited for the predictive simulations required in this work.

Although the use of reduced models makes the control design process simpler, the highly coupled nonlinear nature of the tokamak can potentially lead to unexpected behaviour when controllers tuned and tested on reduced models are experimentally tested. This motivates the intermediate step of conducting closed loop simulations of real-time control laws in an integrated modelling code framework. In this work, such a framework is developed for the TRANSP code. The framework makes use of many of the predictive capabilities of TRANSP mentioned above and includes a new module that enable the stored energy to be predicted based on confinement scaling expressions. A means is provided for performing control calculations based on user-supplied data (controller matrices, target waveforms, etc.). These calculations, along with the acquisition of 'real-time' measurements and manipulation of TRANSP internal variables representing the control systems actuators, are implemented through a hook that allows custom run-specific code to be inserted into the standard TRANSP source code. The framework has the flexibility to simulate a variety of other control designs, and will enable fine-tuning of control laws, studies of robustness to scenario changes, studies of the impact of control laws on parameters not considered in the reduced models used for initial designs, and the demonstration of novel control schemes before devoting experimental time to their implementation. Note that the wall time for the simulations presented in this work is roughly an hour or two per resistive time. Thus, these simulations will not replace

the use of simplified models for initial controller design, but are certainly fast enough to be used for more rigorous testing of control laws and fine-tuning. Use of an integrated modelling framework for such purposes has also been studied in [49], in which real-time profile control algorithms for JET were simulated using the JETTO code. As shown in this work, integrated modelling simulations can also be useful for generating control-oriented models based on simulated data to predict the effectiveness of system identification experiments and, in some cases, may remove the need for dedicated system identification experiments all together. This use of integrated modelling codes has also been studied through the combination of the DINA-CH and CRONOS codes [50] in [51, 52] for the development of control-oriented models of the current profile dynamics in ITER.

1.1. Organization

The paper is organized as follows. In section 2, the computational approach used in the predictive TRANSP simulations is summarized and the modifications necessary for implementing closed loop control within TRANSP are introduced, while the implementation of these modifications is described in section 3. The design and TRANSP simulation of the central safety factor and β_N control algorithms is presented in section 4. Conclusions and future work are discussed in section 5.

2. Overview of computational approach

The predictive TRANSP simulations in this work follow a similar approach to that used in the NSTX-U scenario development work done in [37]. In that work, the inputs to TRANSP were the time histories of the plasma boundary shape, total plasma current, electron temperature and density profiles, and the power, voltage, and geometry of the neutral beam injection. With these inputs, the TRANSP code was used to compute the solution to the poloidal-field equation [53], based on calculations of the bootstrap current, NBCD, and free-boundary equilibrium. TRANSP was configured to compute the bootstrap current from the Sauter model [54] and the NUBEAM code [46] was used to compute the NBCD, with the beam-current shielding factor given by Lin-Liu and Hinton [55].

The free-boundary equilibrium was calculated using the ISOLVER equilibrium code within TRANSP [47, 48]. ISOLVER computes a free-boundary solution to the Grad–Shafranov equation that has boundary and X-point locations that best match a provided target plasma boundary. The target equilibria were generated using the stand-alone version of ISOLVER, based on the NSTX-U coil set. In an iterative procedure, a free-boundary equilibrium solution is obtained, the current and pressure profiles are computed on the new equilibrium, and the equilibrium is recalculated.

In addition to equilibrium calculations, scenario studies require simulation of the ion and electron densities and thermal transport. Because experiments indicate that ion heat transport is reasonably well described by neoclassical theory [8–10, 56], the Chang-Hinton model [57] is used to model the dynamics of the ion temperature. However, because models for electron heat transport, external fuelling, impurity sources, and particle transport are not as well validated, the evolutions of electron temperature and particle densities were not modelled by first-principles calculations.

To handle the remaining unmodelled quantities, the following assumptions were made. First, the electron density profile was taken from an experimental profile measured on NSTX, scaled to achieve a particular Greenwald fraction $f_{GW} = \bar{n}_e/(I_p/\pi a^2)$ [58, 59]. The ion density was calculated by assuming a flat $Z_{eff} = 2$ profile with carbon as the only impurity. The electron temperature was again taken from an experimental profile and scaled to achieve a particular global confinement level. The toroidal rotation profile was also taken from experiment and scaled inversely with the density. The scenario development simulations were run with experimental profiles from five different NSTX discharges to study the effect of profile shape on performance.

2.1. Modifications necessary for closed loop simulations

The modelling approach described above was well-suited for scenario development work in which scans of different densities, temperatures, beam powers, and other parameters were done and the fully-relaxed profiles and performance indicators were compared. However, several modifications to the approach are necessary in order to develop a framework for closed loop simulations.

First, in the above approach, the temperature and density magnitudes were scanned until a particular confinement level and f_{GW} were achieved. This approach is not applicable in closed loop simulations, where it is necessary for the simulation to be constrained to follow a specified confinement level for all time, even as parameters like the plasma current and beam powers are varied, either by preprogrammed waveforms or based on the calculations of a feedback controller. This will ensure that, for example, the temperature used throughout the calculations in TRANSP increases appropriately if the total beam power is increased at the request of a control law. Depending on the nature of the control study, the density may also need to change in response to changes in parameters, either at the request of a feedback controller, or to ensure a particular f_{GW} or particle inventory is maintained throughout the simulation.

Secondly, although the inputs to TRANSP can be time-varying, the waveforms must be specified before initiating the run in the production version of TRANSP. For feedback control studies, it is necessary to update the input data throughout the simulation based on changing plasma parameters and the results of algorithm calculations. This requires both a means to modify TRANSP input data during the simulation and a way to include custom feedback control algorithms that calculate the new input data based on 'real-time' measurements of the plasma state. As the motivation for this work was testing current profile controllers, we have so far focused on enabling online modification of the density, beam powers, total plasma current, and plasma boundary, which are the most likely actuation methods for that particular problem. However, it is planned to extend this framework to enable modification of other parameters, for example the coil currents used by shape control algorithms.

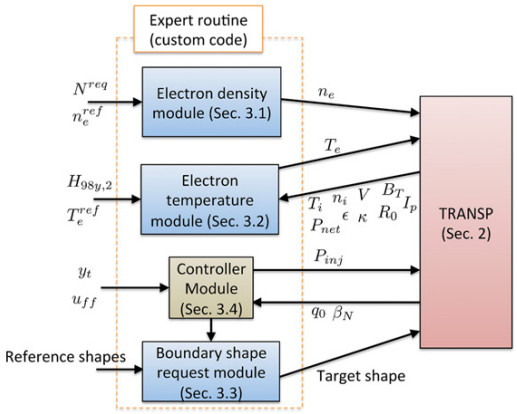

Figure 1. Schematic of Expert routine used to implement closed loop simulations in TRANSP.

3. Expert routine for feedback control simulations

The modifications necessary for closed loop simulations have been implemented through the so-called Expert routine. This routine is a hook, called at various places throughout the TRANSP source code, which can be used to insert run-specific custom code into the production version of TRANSP. A detailed description of the Expert routine developed for feedback control is provided in this section and a schematic is given in figure 1.

3.1. Electron density specification

The electron density is taken to be of the form

$$n_{\rm e}(\hat{\rho},t) = n_{\rm e,0}(t) n_{\rm e}^{\rm ref}(\hat{\rho}), \tag{1}$$

where $n_{\rm e}^{\rm ref}$ is a user-supplied reference profile and $n_{\rm e,0}$ is a time-varying scale factor used to ensure that the particle inventory, N, follows a conservation equation. The desired particle inventory, $N^{\rm req}$, can either be specified as a function of time or calculated based on TRANSP internal variables to achieve a specified line-averaged density or Greenwald fraction waveform. At the start of each TRANSP transport time step (covering the time interval (t_a, t_b)), the desired inventory is calculated and the applied particle inventory is evolved using the equation

$$N_b = N_a + (t_b - t_a)(N^{\rm req} - N_a)/\tau_N, \tag{2}$$

where τ_N is an approximate density confinement time. For the simulations in this work, $\tau_N = 0.1$s (approximately a few multiples of the energy confinement time) was used. This simplified model approximates the presence of a particle control algorithm modifying the dynamics of the particle inventory through, for example, fuelling and pumping. By including a conservation equation for particle inventory instead of assigning the density *a priori*, the density changes appropriately in response to changes in plasma volume. The presented approach was suitable for this work, but (2) could be replaced by a more complex physics-based conservation equation that explicitly accounts for fuelling sources and effects like recycling in the future.

For a particular inventory, N, the scale factor $n_{\rm e,0}$ is calculated from

$$n_{\rm e,0} = \frac{N}{\int_0^1 n_{\rm e}^{\rm ref} \frac{\partial V}{\partial \hat{\rho}} \, {\rm d}\hat{\rho}}. \tag{3}$$

Because TRANSP typically obtains the electron density from an input file, a call to the Expert routine must be made just after each time TRANSP accesses this input data. At each of these calls, the Expert file code interpolates the density profile for the appropriate time (TRANSP may look for density information at a time other that t_a or t_b during a particular transport step) and replaces the TRANSP internal variable for electron density with the calculated one.

3.2. Electron temperature specification and global confinement constraint

The electron temperature is taken to be of the form

$$T_{\rm e}(\hat{\rho},t) = T_{\rm e,0}(t) T_{\rm e}^{\rm ref}(\hat{\rho}), \tag{4}$$

where $T_{\rm e}^{\rm ref}$ is a user-defined reference profile and $T_{\rm e,0}$ is used to scale the temperature to maintain the stored energy predicted from a zero-dimensional (0D, volume averaged) energy balance. At the beginning of each transport step ($t = t_a$), the value of the thermal stored energy $W_{\rm th}$ at the next step ($t = t_b$) is calculated from the power balance (discretized using the Euler method)

$$W_{{\rm th},b} = W_{{\rm th},a} + (t_b - t_a)\left(-\frac{W_{{\rm th},a}}{\tau_E} + P_{\rm net}\right), \tag{5}$$

where τ_E is the confinement time and $P_{\rm net}$ is the net heating source calculated as the sum of all heating and loss terms from the thermal ion and electron power balance calculated by TRANSP. The confinement time is calculated based on one of two different assumptions. The first is the $H_{98y,2}$ scaling expression [60], given by

$$\tau_{98y,2} = H_{98y,2} 0.0562 I_{\rm p}^{0.93} B_{\rm T}^{0.15} \bar{n}_{\rm e}^{0.41} P_{\rm Loss,th}^{-0.69} R_0^{1.97} \epsilon^{0.58} \kappa^{0.78}. \tag{6}$$

The second is a ST expression [7], given by

$$\tau_{\rm ST} = H_{\rm ST} 0.1178 I_{\rm p}^{0.57} B_{\rm T}^{1.08} \bar{n}_{\rm e}^{0.44} P_{\rm Loss,th}^{-0.73}. \tag{7}$$

In both expressions, $I_{\rm p}$ is the plasma current in MA, $B_{\rm T}$ is the toroidal magnetic field in T, $\bar{n}_{\rm e}$ is the line-averaged electron density in $\#/{\rm m}^3 \times 10^{19}$, R_0 is the major radius in m, ϵ is the inverse aspect ratio, and κ is the elongation. The loss power $P_{\rm Loss,th}$ is in MW and is defined in [7] as total input heating power less ${\rm d}W/{\rm d}t$ and fast ion losses through charge-exchange, bad orbits, and shine-through. The factors $H_{98y,2}$ or $H_{\rm ST}$ are interpolated from a user-supplied waveform.

Because TRANSP typically obtains the electron temperature from an input file, a call to the Expert routine is made just after each time TRANSP accesses the temperature input data. At each of these calls, the Expert file code interpolates the thermal stored energy $W_{\rm th}$ for the appropriate time based on $W_{{\rm th},a}$ and $W_{{\rm th},b}$, the predicted values at t_a and t_b and calculates the required scale factor $T_{\rm e,0}$ for the reference profile. Noting that

$$E_{\rm th} = \tfrac{3}{2}\left[n_{\rm e} T_{\rm e} + n_{\rm i} T_{\rm i}\right], \tag{8}$$

and using the volume average formula

$$\langle x \rangle = \frac{1}{V} \int_0^1 x \frac{\partial V}{\partial \hat{\rho}} \, \mathrm{d}\hat{\rho}, \tag{9}$$

the volume averaged stored energy can be calculated as

$$\langle E_{\mathrm{th}} \rangle = \frac{W_{\mathrm{th}}}{V} = \frac{3}{2} \left[T_{\mathrm{e},0} \langle n_{\mathrm{e}} T_{\mathrm{e}}^{\mathrm{ref}} \rangle + \langle n_{\mathrm{i}} T_{\mathrm{i}} \rangle \right]. \tag{10}$$

This can be solved for $T_{\mathrm{e},0}$, yielding

$$T_{\mathrm{e},0} = \frac{\frac{2}{3} \langle E_{\mathrm{th}} \rangle - \langle n_{\mathrm{i}} T_{\mathrm{i}} \rangle}{\langle n_{\mathrm{e}} T_{\mathrm{e}}^{\mathrm{ref}} \rangle}. \tag{11}$$

In these calculations, the n_{i}, n_{e}, and T_{i} profiles are taken from the TRANSP internal variables at the current time step. Recall from section 2 that T_{i} is calculated using the Chang-Hinton model, and n_{i} is calculated by assuming a Z_{eff} profile and carbon as the only impurity.

3.3. Equilibrium specification

The free-boundary equilibrium code ISOLVER can be operated in either 'circuit equation mode', in which the coil currents are driven from input data, or in 'least squares mode', in which the coil currents are calculated at each step to best fit a prescribed plasma boundary. While the former mode will be exploited in the future for testing feedback control algorithms for the shape, we have focused on using the latter operating mode in this work, i.e. we vary the target plasma boundary, but do not consider the design of the shape controller itself. Passive conducting structures, which will influence shape control through induced eddy currents, are not considered in this simulation mode, but will be included in future shape control studies using the 'circuit equation mode'. At the start of each magnetic geometry calculation step, just after the inputs to ISOLVER are set up, the Expert routine is called and the existing plasma boundary reference and total plasma current value are replaced with the values requested by the control algorithm. In order to avoid crashes caused by these inputs varying too rapidly, the requests are first filtered with a low-pass filter with time constant τ_G ($\tau_G = 0.05$ s was used throughout the simulations in this work).

3.4. Control algorithm implementation

A flexible control algorithm has been implemented that allows testing of control laws that take the form of a discrete state-space system with a nonlinear transformation of the output. This algorithm was chosen because it accommodates many of the proposed current profile designs, but other custom algorithms can be implemented within the framework. A schematic of the framework and details of the implementation are provided in appendix.

4. Control of q_0 and β_{N} with total beam power and outer gap size

In this section, the design and TRANSP testing of a novel q_0 and β_{N} controller that uses the total beam power and outer gap of the plasma boundary as the manipulated variables is presented. To implement the outer-gap as an actuator in TRANSP, the stand-alone version of ISOLVER was used to generate two magnetohydrodynamic (MHD) equilibria: one with a gap size of 0.05 m and the other with a gap size of 0.20 m. The equilibria are compared in figure 2. Highly elongated plasma shapes like these are among those planned for NSTX-U [1, 37], and similar values of elongation and aspect ratio have been achieved in experiments on NSTX [15, 18]. Given a requested outer-gap size, the Expert routine was programmed to calculate the target plasma boundary shape by interpolating between the plasma boundary shapes associated with these two reference equilibria. Two different control law design approaches are considered, a multi-input-multi-output (MIMO) controller and a design that splits the system into two single-input-single-output loops. The two schemes are depicted in figure 3.

4.1. MIMO design approach

In this section, the problem of controlling q_0 and β_{N} using the total beam power and outer-gap-size is approached using modern control theory, which enables the constructive design of control laws for MIMO systems. A system identification process was used to develop a linear state-space response model of the system, and this model was then used to design an optimal control law.

A linear state-space response model was sought of the form

$$\begin{aligned} \delta x_{k+1} &= A \delta x_k + B u_{\mathrm{fb,k}}, \\ \delta y_k &= C \delta x_k + D u_{\mathrm{fb,k}}. \end{aligned} \tag{12}$$

In this model, the physical actuator levels $u = [P_{\mathrm{inj}}, g_{\mathrm{outer}}]^T$ are given by $u = u_{\mathrm{ff}} + u_{\mathrm{fb}}$ where u_{ff} is a feedforward reference value and u_{fb} is the deviation from the reference. Similarly, the measurements of the system outputs $y = [q_0, \beta_{\mathrm{N}}]^T$ are given by $y = y_{\mathrm{ff}} + \delta y$, where y_{ff} is the reference value associated with u_{ff} and δy is the deviation due to initial condition errors and the actuator deviation u_{fb}. Note that, in experiments, these measurements will be obtained from MSE constrained rtEFIT reconstructions of the plasma equilibrium. In order to identify the system matrices A, B, C, and D for use in a model-based control design, a dedicated set of system identification experiments was conducted. First, a four second long simulation (with $I_{\mathrm{p}} = 0.6$ MA, $B_{\mathrm{T}} = 1.0$ T, $N^{\mathrm{req}} = 5.05 \times 10^{20}$, and with $n_{\mathrm{e}}^{\mathrm{ref}}$ and $T_{\mathrm{e}}^{\mathrm{ref}}$ taken from NSTX shot 133964) was completed using the constant actuator values set at the mean of the actuator range ($g_{\mathrm{outer}} = 0.125$ m, $P_{\mathrm{inj}} = 6.3$ MW distributed evenly among the six beam lines), representing u_{ff}. The choice of scenario was motivated by the study of scenarios with good prospects for current profile controllability done in [37]. The steady-state value of q_0 and β_{N} during this simulation was then taken to be y_{ff}. In the second simulation, the actuator values were modulated around u_{ff} in order produce a deviation δy. In order to excite a range frequencies for better identification of the model parameters, the modulation u_{fb} was chosen as a set of two pseudorandom binary sequences scaled by an amplitude $A_{\mathrm{ID}} = [2, 0.075]^T$. The combined signal $u = u_{\mathrm{ff}} + u_{\mathrm{fb}}$ used in the identification simulation is shown in figure 4. The dataset $(u_{\mathrm{fb}}, \delta y)$ resulting from the 10 s long simulation was then split into two intervals

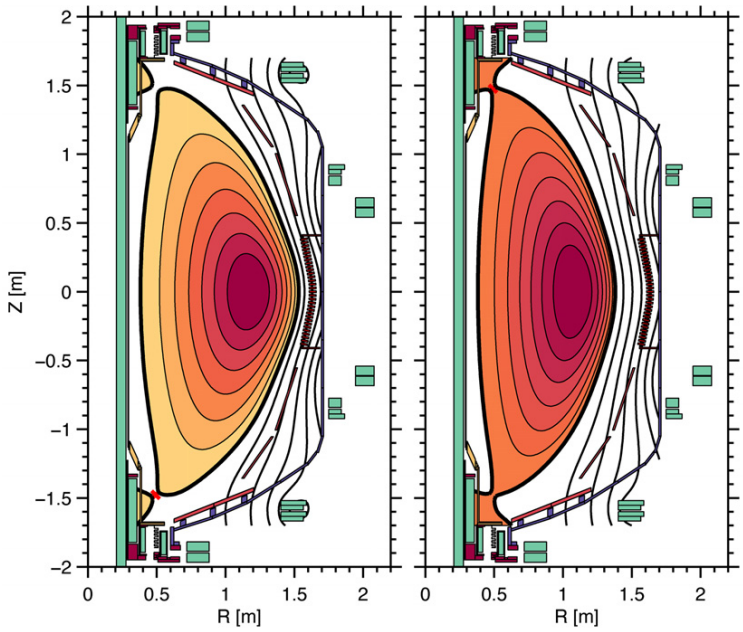

Figure 2. Cross-section of NSTX-U conducting structures comparing the two reference MHD equilibria with (left) $g_{\text{outer}} = 0.05$ m and (right) $g_{\text{outer}} = 0.20$ m. (Note: conducting structures were not included in the equilibrium calculations, but will be considered in future work when shape control algorithms are added to the closed loop TRANSP framework).

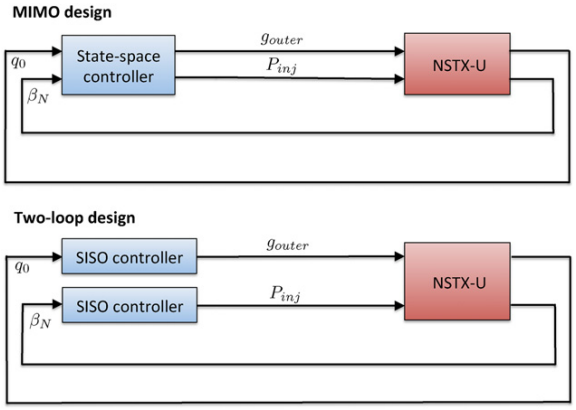

Figure 3. Schematics of the MIMO and two-loop control design approaches.

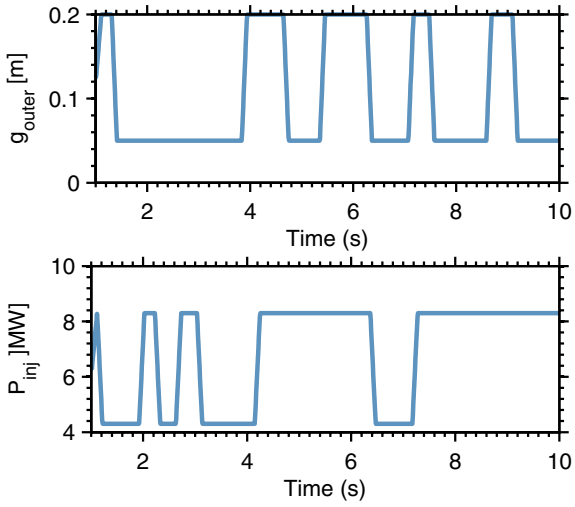

Figure 4. Actuator requests used in the system identification simulation.

$t_1 = (1.0, 6.0)$ s and $t_2 = (6.0, 10.0)$ s, so that one set could be used for parameter estimation and the other could be use for model validation. The prediction error method [61] for state-space model identification, part of the Matlab System Identification Toolbox [62], was used to identify the optimal system matrices for a prescribed number of states n_x (model-order) that best matched the estimation data set. The optimal choice of model-order was then found by identifying a set of models for a small range of n_x, simulating the identified models using the inputs from the validation dataset, and comparing how well each model predicted the output of the validation dataset. Models with too few states fail to capture the dynamics of the system, while models with excessive states overfit the noise in the estimation data set, degrading prediction of the validation dataset. A comparison of the output of the optimal model, which was found to be of order four, to the validation data is shown in figure 5, showing good agreement in q_0 and excellent agreement in β_N.

The identified model was then used to design a linear-quadratic-Gaussian servo controller [63]. This type of controller minimizes a cost function of the form

$$J = E\left\{\lim_{N\to\infty}\sum_{k=0}^{N}\left(\left[\delta x^T, u_{\text{fb}}^T\right] Q_{xu}\begin{bmatrix}\delta x\\ u_{\text{fb}}\end{bmatrix} + x_i^T Q_i x_i\right) T\right\}, \tag{13}$$

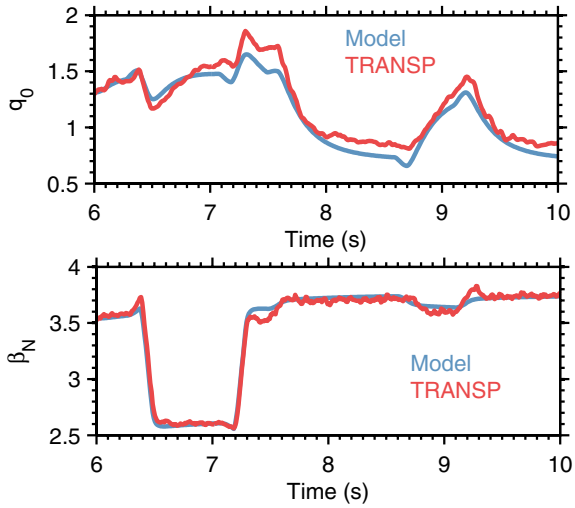

Figure 5. Comparison of output predicted by the identified model to the actual output of the validation dataset.

where x_i is the integral (approximated by the Euler forward difference) of the tracking error, for a system of the form

$$\delta x_{k+1} = A\delta x_k + Bu_{\mathrm{fb},k} + w_k,$$
$$\delta y_k = C\delta y_k + Du_{\mathrm{fb},k} + v_k, \qquad (14)$$

where the process noise w and measurement noise v are Gaussian white noise signals with covariance given by a matrix Q_{wv}. The controller optimizes the use of actuators according to the weights in Q_{xu}, which are free design parameters, and also ensures reference tracking with the 'integral action' tailored by choice of the free design parameters in Q_i. A Kalman filter is embedded in the resulting control law, which optimally estimates the unmeasured states δx based on the measurements δy, taking into account the process and measurement noise levels. The identified model was simulated using Simulink in order to tune the free design parameters to achieve a desired system response. A simple back-calculation type anti-windup scheme was implemented (see [64] for more details) to keep the actuator requests from winding up far beyond their saturation levels by feeding back a signal proportional to an integral of the unrealized actuation.

The controller was then tested in a TRANSP simulation using the proposed simulation framework (again with $I_\mathrm{p} = 0.6\,\mathrm{MA}$, $B_\mathrm{T} = 1.0\,\mathrm{T}$, $N^\mathrm{req} = 5.05 \times 10^{20}$, and with $n_\mathrm{e}^\mathrm{ref}$ and $T_\mathrm{e}^\mathrm{ref}$ taken from NSTX shot 133964). Time-dependent results of the closed loop simulation of the MIMO control law are shown in figure 6. Figures 6(*a*) and (*b*) show the successful tracking of the time-varying targets for q_0 and β_N. Neither q_0 or β_N exhibit significant overshoot or oscillations (other than those caused by numerical noise). The beam-driven, bootstrap, and non-inductive current fractions are compared in figure 6(*c*). While the bootstrap current increased at the second operating point, the beam-driven fraction decreased. There is therefore little change in the total non-inductive fraction. The response of the actuators g_outer and P_inj are shown in figures 6(*d*) and (*e*), respectively. Finally, the density, shown in figure 6(*f*), increased as the outer-gap-size was increased and the plasma volume decreased, since the particle inventory was held fixed during the simulation.

Profiles at the end of the two target steps are compared in figure 7. The first operating point had a low q_0 and the safety factor profile was monotonic as a result of low bootstrap current and beam-driven current peaked on-axis. At the second operating point, the bootstrap current increased slightly while the beam-driven current decreased on-axis (inside $\hat{\rho} = 0.35$). The combination of these two effects made the total non-inductive current drive distribution peaked further off-axis, causing an increase in q_0. The coil currents and voltages needed to produce the requested plasma boundary shapes are depicted in figures 8, and 9, respectively, showing that the expected currents are within physical limits (see [65]), implying the proposed control approach should be experimentally feasible.

To study the robustness of the control law to changes in electron density and temperature profile shapes, the simulation was repeated with $T_\mathrm{e}^\mathrm{ref}$ and $n_\mathrm{e}^\mathrm{ref}$ taken from NSTX shot 121123 (instead of 133964 as in the system identification and first testing simulations). Results of this test are shown in figure 10. A comparison of the reference electron temperature and density profiles used in the perturbed case (from 121123) and the design case (from 133964) is shown in figures 10(*a*) and (*b*). The temperature profile is more narrow in the perturbed case, and the density profile exhibits a region with a reduced gradient. Figures 10(*c*) and (*d*) show that the controller performance is not significantly affected by the profile change (compare to the results shown in figure 6). The q profiles achieved at the end of the simulations ($t = 7.0\mathrm{s}$) are compared in figure 10(*e*), showing that although the controller forces q_0 to match, the (uncontrolled) shape of the q profile differs. This change in shape can be attributed to the difference in the bootstrap current profiles, compared in figure 10(*f*), that resulted from altering the electron temperature and density profile shapes.

4.2. Two loop design approach

The results of the system identification simulation indicated that the response of β_N is dominated by the beam power and the response of q_0 is highly dependent on g_outer (note in figure 5, for example, that β_N remains approximately constant after $t = 7.25\,\mathrm{s}$, despite modulation of g_outer). This observation, along with the large timescale difference between the evolution of q_0 and the evolution of β_N, suggests that a two-loop control structure may be appropriate. Although this approach neglects some of the coupling in the system, single-input-single-output control laws are more intuitive and easier to retune. The system identification procedure is also less involved than the previous case, which may be desirable if experimental time for control development is very limited (note that this point may be made irrelevant if it is found that system identification based on TRANSP predictive simulations alone is sufficient for control design). First, a controller for β_N using the total beam power as the manipulated variable was designed based on a simplified model of the stored energy dynamics. Next a controller for q_0 using the outer gap as the manipulated variable was designed based on an identified approximate model for the central safety factor dynamics. PID controllers were designed for each of these single-input-single-output loops. A PID controller is a generic feedback control loop structure that calculates corrective action to minimize the error between a controlled

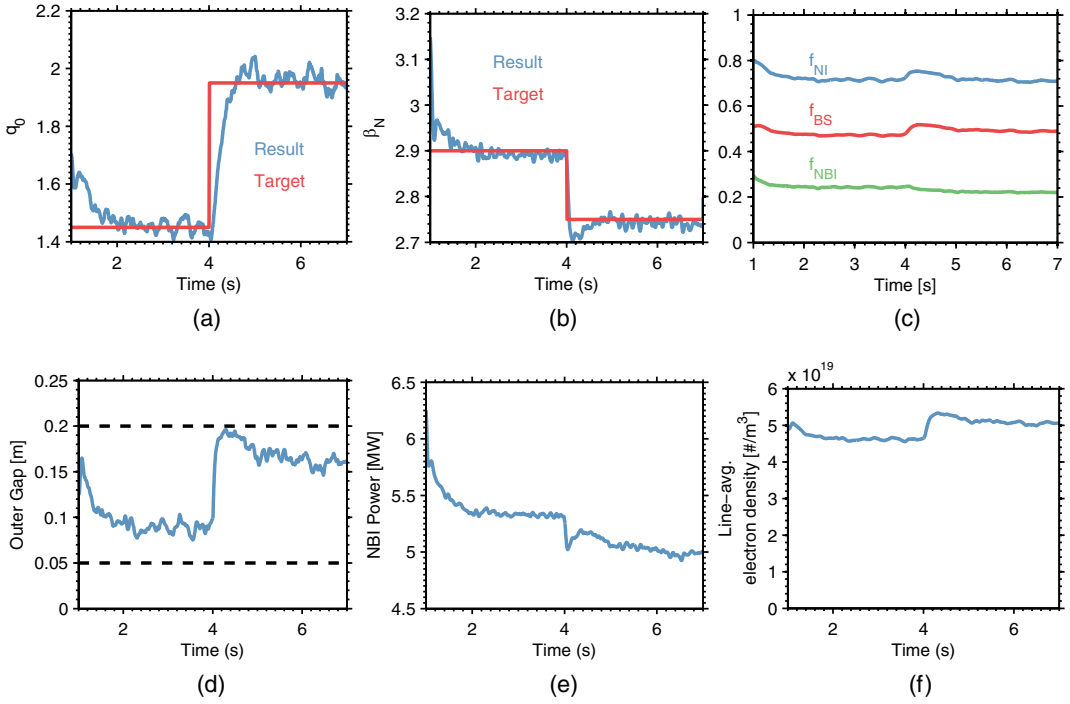

Figure 6. Results of closed loop simulation of the MIMO control law: (*a*) q_0 result compared to target, (*b*) β_N compared to target, (*c*) non-inductive current fractions, (*d*) outer gap, (*e*) injected power and (*f*) electron density.

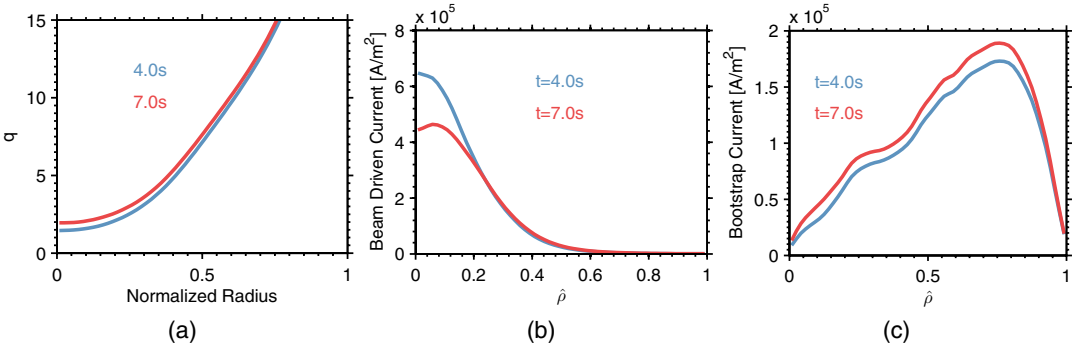

Figure 7. Results of closed loop simulation of the MIMO control law: (*a*) q profiles, (*b*) beam driven current profiles and (*c*) bootstrap current profiles.

variable and a desired set point by weighting the error, its integral over time, and its time derivative. This corrective action can be written as

$$u_{\rm fb}(t) = K_P u_c(t) + K_I \int_0^t u_c(\tau)\,{\rm d}\tau + K_D \frac{{\rm d}u_c(t)}{{\rm d}t}. \quad (15)$$

The free gain parameters K_P, K_I, and K_D for each loop were tuned based on approximate models of the dynamics of the system. For the β_N loop, noting that $\beta_N = 100\frac{\beta_T a B_T}{I_p}$, where $\beta_T = \frac{2\mu_0(2/3W)}{VB_T^2}$, the dynamics were approximated by

$$\begin{aligned}\dot{\beta}_N &= \frac{400a\mu_0}{3I_{\rm p}B_{\rm T}V}\dot{W} + \frac{400\mu_0 W}{3I_{\rm p}B_{\rm T}V}\dot{a} - \frac{400a\mu_0 W}{3I_{\rm p}B_{\rm T}V^2}\dot{V} \\ &\quad - \frac{400a\mu_0 W}{3I_{\rm p}B_{\rm T}^2V}\dot{B}_{\rm T} - \frac{400a\mu_0 W}{3I_{\rm p}^2B_{\rm T}V}\dot{I}_{\rm p} \\ &= \frac{400a\mu_0}{3I_{\rm p}B_{\rm T}V}\left(-\frac{W}{\tau_E} + P_{\rm net}\right) + \frac{400\mu_0 W}{3I_{\rm p}B_{\rm T}V}\dot{a} \\ &\quad - \frac{400a\mu_0 W}{3I_{\rm p}B_{\rm T}V^2}\dot{V} - \frac{400a\mu_0 W}{3I_{\rm p}B_{\rm T}^2V}\dot{B}_{\rm T} - \frac{400a\mu_0 W}{3I_{\rm p}^2B_{\rm T}V}\dot{I}_{\rm p}. \end{aligned} \quad (16)$$

We consider the heating to be dominated by the injected beam power, i.e. $P_{\rm net} \approx P_{\rm inj}$, define $u = \frac{400a\mu_0}{3I_{\rm p}B_{\rm T}V}P_{\rm inj}$ as a virtual actuator, and lump the last four terms into a single disturbance term denoted by d, to write

$$\dot{\beta}_{\rm N} = -\frac{\beta_{\rm N}}{\tau_E} + u + d. \quad (17)$$

We consider a set of reference trajectories u_{ff} and d_{ff}, and the associated evolution of $\beta_{\rm N}$, denoted $\beta_{N,\rm ff}$, which is governed by

$$\dot{\beta}_{N,\rm ff} = -\frac{\beta_{N,\rm ff}}{\tau_{E,\rm ff}} + u_{\rm ff} + d_{\rm ff}. \quad (18)$$

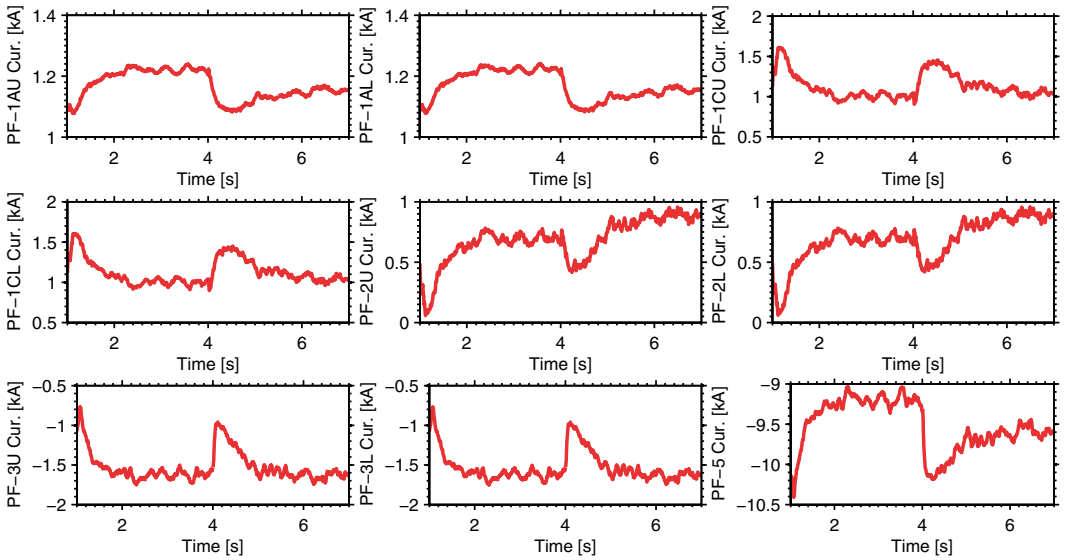

Figure 8. Poloidal field coil currents during closed loop simulation of the MIMO control law. Note that each coil has a different maximum current, but the maximum is at least 13 kA for each.

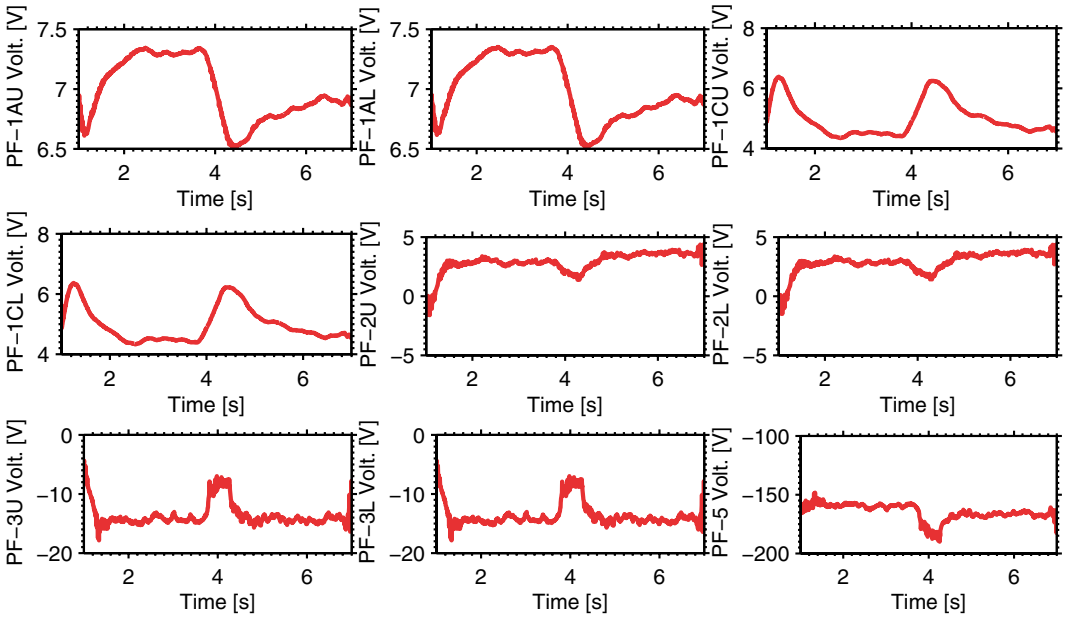

Figure 9. Poloidal field coil voltage during closed loop simulation of the MIMO control law. Note that each coil has a different maximum available voltage, but the maximum is at least 1 kV for each.

Denoting deviations of a signal z from its reference value as $\delta z = z_{\rm ff} - z$, the dynamics of $\delta\beta_{\rm N}$ can be written as

$$\begin{aligned}\dot{\delta\beta}_N &= -\theta\beta_{\rm N} + u + d + \theta_{\rm ff}\beta_{N,\rm ff} - u_{\rm ff} - d_{\rm ff} \\ &= -\theta\delta\beta_{\rm N} - \delta\theta\beta_{N,\rm ff} + \delta u + \delta d, \end{aligned} \tag{19}$$

where $\theta = \frac{1}{\tau_E}$. Noting that $u = u_{\rm ff} + u_{\rm fb}$, i.e., $u_{\rm fb} = -\delta u$, we choose the control law

$$u_{\rm fb} = \delta d - \delta\theta\beta_{N,\rm ff} + K_{P,\beta}\delta\beta_{\rm N} + K_{I,\beta}\int_0^t \delta\beta_{\rm N} d\tau. \tag{20}$$

where $K_{P,\beta} > 0$ and $K_{I,\beta} > 0$. The first two terms cancel the effect of disturbances, while the last two terms add proportional and integral feedback, increasing speed of response and ensuring disturbance rejection (and target tracking if $\delta\beta_{\rm N}$ is replaced by $\beta_{N,r} - \beta_{\rm N}$ in the control law, where $\beta_{N,r}$ is the desired target). While the disturbance terms could be measured, or at least estimated in real-time, it was found through simulation that treating them as unmeasured and using only a PI controller was sufficient for this design.

The design parameters $K_{P,\beta}$ and $K_{I,\beta}$ were tuned to achieve a desirable response through Simulink simulations of the system.

The dynamics of q_0 were modelled by a first-order-plus-dead-time (FOPDT) model, which can be written in the

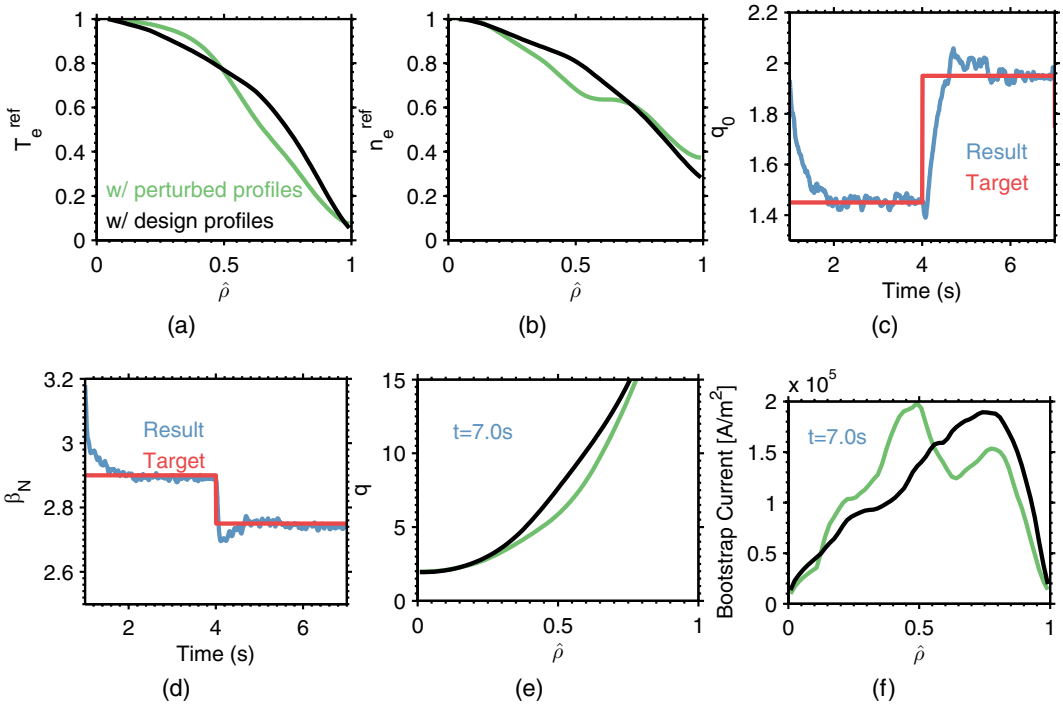

Figure 10. Results of the closed loop simulation of the MIMO control law with modified reference profiles: (*a*) comparison of modified electron temperature reference profile to the one used for design, (*b*) comparison of modified and design electron density reference profiles, (*c*) q_0 result compared to target, (*d*) β_N compared to target, (*e*) comparison of q profiles at $t = 7.0$ s in each case, and (*f*) comparison of bootstrap current profiles at $t = 7.0$ s in each case.

time-domain as

$$\dot{y}(t) = -\frac{y(t) + Ku(t - L)}{T}, \tag{21}$$

where K is the static gain, T is the time constant, and L is the dead time. These parameters were identified by studying the response of the output to a step change in the input. A TRANSP simulation of an NSTX-U discharge with $I_p = 600$ kA and $B_T = 1.0$ T was done in which the outer-gap was held fixed at 0.05 m until a steady value of q_0 was reached, at which point the outer gap was stepped to 0.20 m. During the simulation, the electron particle inventory was fixed at 5.05×10^{20} electrons and the β_N controller regulated the plasma around $\beta_N = 2.7$. The results of the simulation are shown in figure 11. Figure 11(*a*) shows the outer gap, while figures 11(*b*) and (*a*) show the injected beam power and line-averaged density needed to maintain the specified β_N and particle inventory. In 11(*a*), it can be seen that the safety factor profile is increased as a result of the beam current drive moving off axis (figure 11(*b*)) and the increase in bootstrap current (figure 11(*c*)). As seen in figure 11(*d*), the β_N controller successfully kept β_N near its target value. The Greenwald fraction dropped slightly due to the reduction in plasma minor radius. This reduction is shown in figure 11(*f*) along with the increase in elongation (which contributes to the increased bootstrap current) and the decrease in volume. The increase in beam current drive efficiency and bootstrap current led to an increase in the non-inductive fraction, as seen in figure 11(*e*). A curve fitting procedure was used to determine the optimal FOPDT model parameters to match the response of q_0 to the step change in outer gap. The step response is compared with the identified model in figure 12, showing good agreement.

The FOPDT model enables the design parameters of the feedback controller to be tuned using the Ziegler–Nichols PID tuning method, a well-known heuristic design algorithm for selecting the gains based on the parameters of the FOPDT model [66], which has been used previously for NSTX control development in [24]. The gains are provided in table 1. It was found that a PI controller ($K_D = 0$) was sufficient to achieve good performance in this case (the parameters were modified from this starting point empirically to improve the system performance based on the results of Simulink simulations of a discrete-time version of the two-loop control law). The anti-windup design was the same as that used for the MIMO control simulations.

A closed loop TRANSP simulation of the two-loop controller was performed using the same simulation parameters as those used for the model identification. The controller was activated at 1s and given a time-varying target that started at $q_0 = 1.6$ between $t = 1$s and 4s, then stepped to $q_0 = 3.0$ from 4s to the end of the simulation.

Time-dependent results of the closed loop simulation are shown in figure 13. In figures 13(*a*) and (*b*) the successful tracking of the time-varying targets for q_0 and β_N is evident. The response of q_0 is much faster than the open loop equilibration time, and neither q_0 or β_N exhibit significant overshoot or oscillations (other than those caused by numerical noise). One exception to this is the response of q_0 to the step change in target at $t = 4.0$ s. The response to this target change was slower than the others due to the saturation of the outer-gap

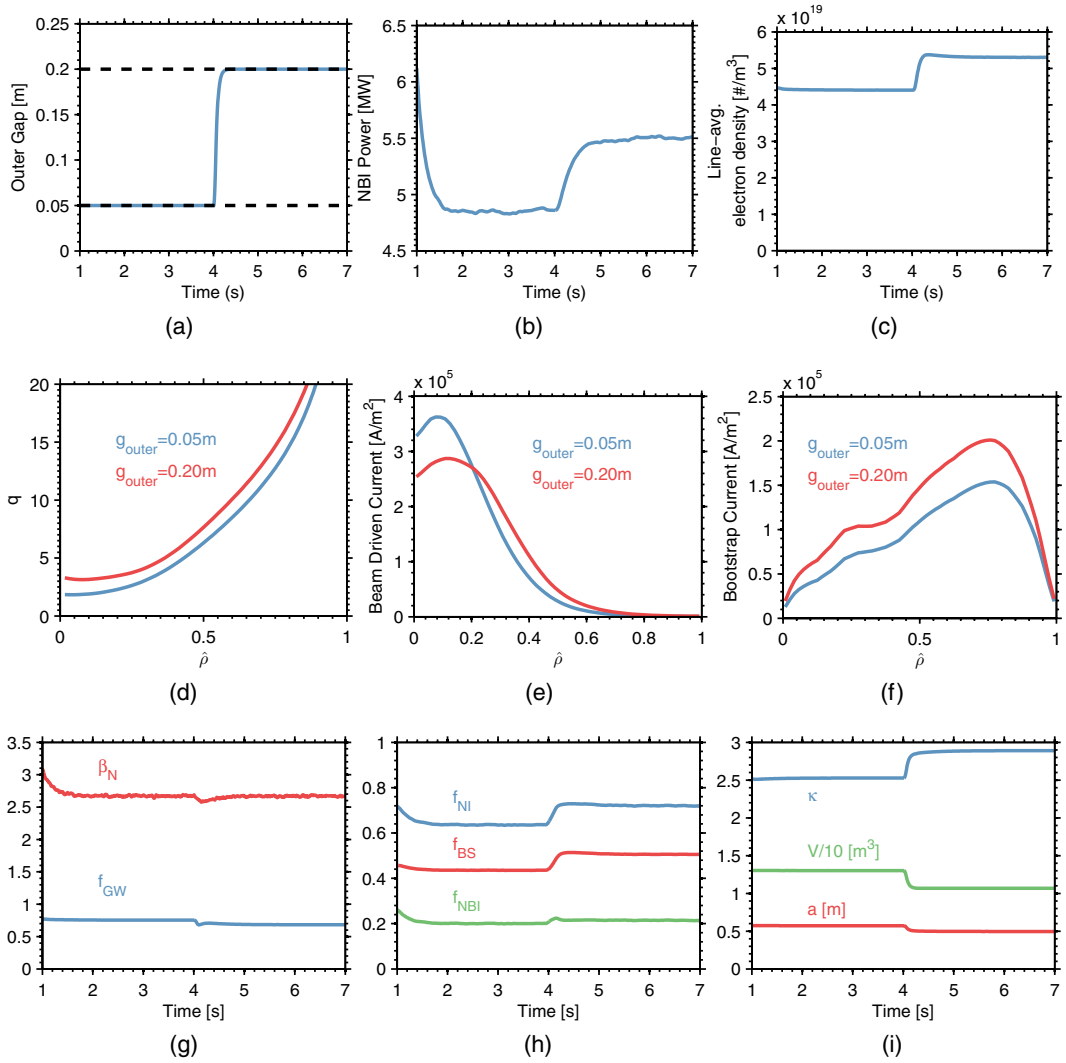

Figure 11. Results of open loop simulation used for system identification for the two-loop control scheme: (*a*) outer gap, (*b*) injected beam power, (*c*) line-averaged electron density, (*d*) q profile, (*e*) beam driven current drive, (*f*) bootstrap current, (*g*) β_N and f_{GW}, (*h*) current fractions, and (*i*) shape related parameters.

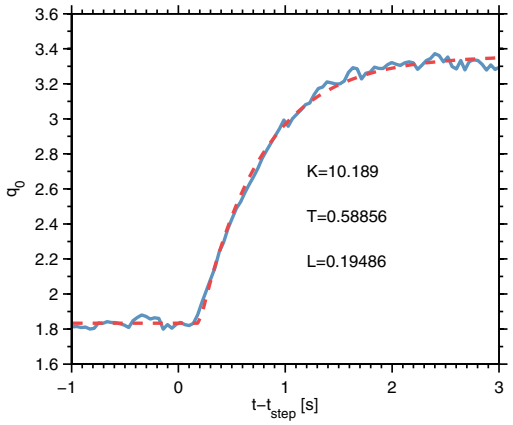

Figure 12. Response of q_0 to a step change in the outer gap.

Table 1. Ziegler and Nichols PID controller gains for FOPDT systems.

Controller type	K_P	K_I	K_D
P	$\frac{1}{K}\frac{T}{L}$	—	—
PI	$\frac{0.9}{K}\frac{T}{L}$	$\frac{K_P}{3.33L}$	—
PID	$\frac{1.2}{K}\frac{T}{L}$	$\frac{K_P}{2.0L}$	$K_P 0.5L$

at its maximum allowed value, as can be seen in figure 13(*d*). For the rest of the simulation, the outer-gap request did not saturate, although it settled at a value very close to the limit after the step change in the target at $t = 7.0$ s. The beam-driven, bootstrap, and non-inductive current fractions are compared in figure 13(*c*). Each of the quantities increased as the operating points were changed. Though the quantities have complex nonlinear dependence on many plasma parameters, the increase in bootstrap current fraction is likely due primarily

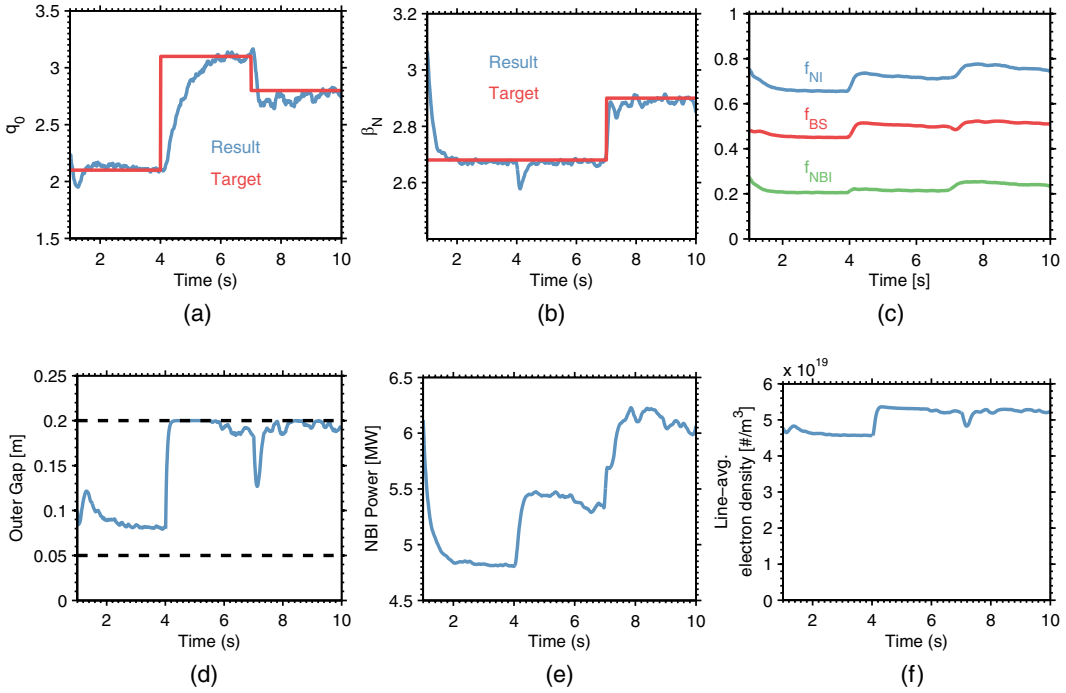

Figure 13. Results of closed loop simulation of the two-loop control scheme: (*a*) q_0 result compared to target, (*b*) β_N compared to target, (*c*) non-inductive current fractions, (*d*) outer gap, (*e*) injected power, and (*f*) electron density.

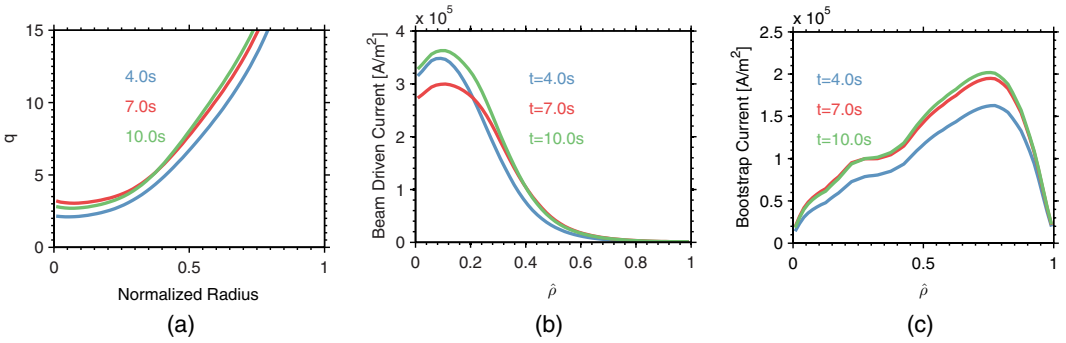

Figure 14. Results of closed loop simulation of the two-loop control scheme: (*a*) q profiles, (*b*) beam driven current profiles, and (*c*) bootstrap current profiles.

to the increase in elongation associated with the larger outer-gap requested after $t = 4.0$ s, while the increase in beam-driven fraction is due primarily to the increase in NBI power required to track the β_N target after $t = 4.0$ s and again after $t = 7.0$ s, as shown in figure 13(*e*). Finally, the density, shown in figure 13(*f*), increased as the outer-gap-size was increased and the plasma volume decreased, since the particle inventory was held fixed during the simulation.

Profiles at the end of each target step are compared in figure 14. The first operating point had a low q_0 and was very slightly reverse-shear, due to low bootstrap current and beam-driven current peaked on-axis. At the second operating point, the bootstrap current increased significantly while the beam-driven current decreased on-axis and increased outside of $\hat{\rho} = 0.25$. This resulted in a much higher q_0, and a more reverse-shear safety factor profile. For the third operating point, the beam-driven-current outside of $\hat{\rho} = 0.35$ matched closely with that of the second operating point, while the on-axis current drive as increased, even above that of the first operating point. The bootstrap current increased slightly over the second operating point level. The net result was an decrease in q_0 and a flatter safety factor profile. The coil currents and voltages needed to produce the request plasma boundary shapes are shown in figures 15 and 16, respectively. The currents and voltages are well within the limits [65], again implying the proposed control approach should be experimentally feasible.

4.3. Discussion

From the simulations results shown here, good performance was obtained using both the MIMO optimal controller and two loop control design. From the perspective of an operator, this is desirable, as it indicates the two loop structure, with a small number of free parameters that can be adjusted intuitively

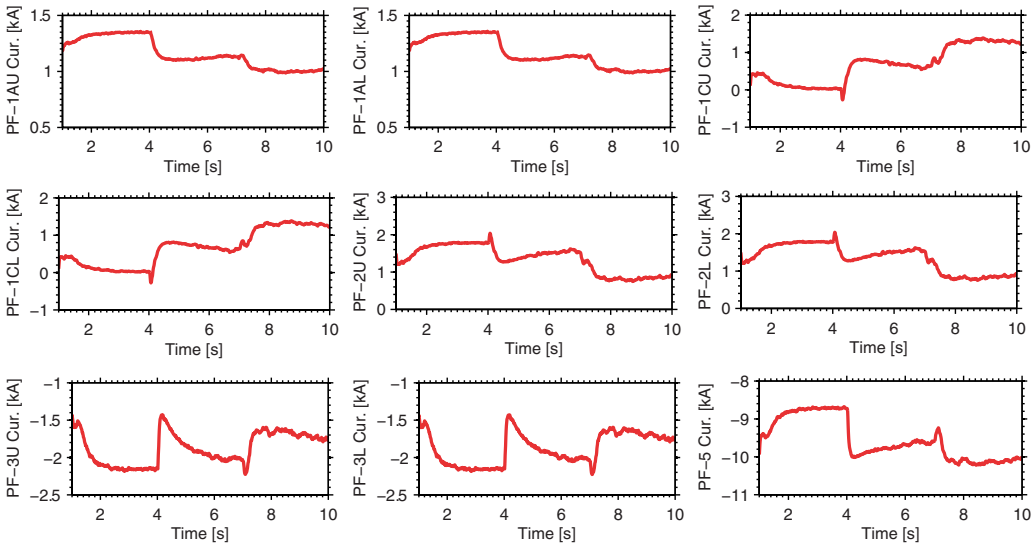

Figure 15. Poloidal field coil currents during closed loop simulation of the two-loop control scheme. Note that each coil has a different maximum current, but the maximum is at least 13 kA for each.

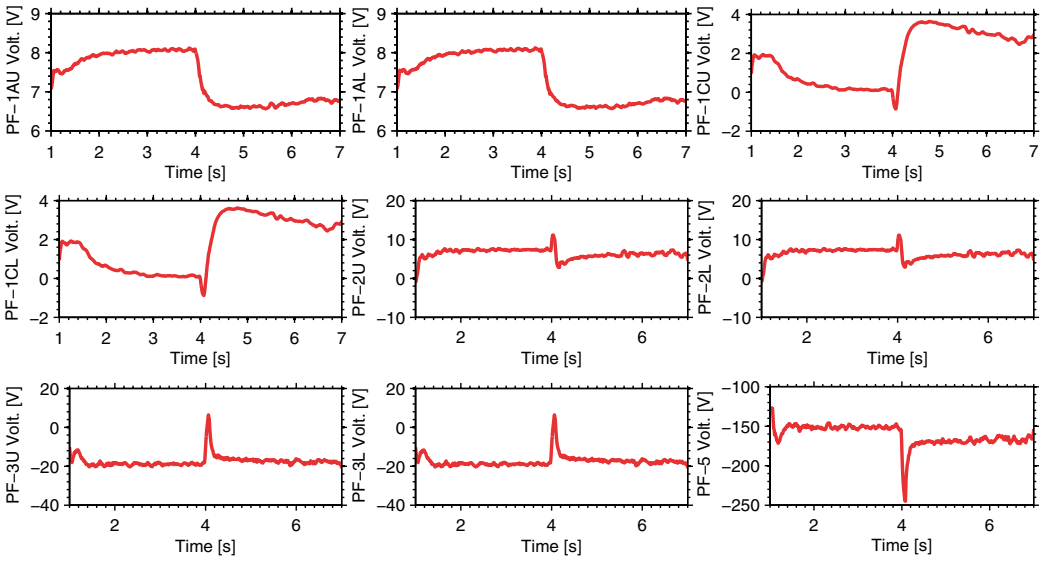

Figure 16. Poloidal field coil voltages during closed loop simulation of the two-loop control scheme. Note that each coil has a different maximum available voltage, but the maximum is at least 1 kV for each.

between shots, may work well in experiments. However, the optimal design provides a more systematic algorithm for designing a stabilizing controller, is well suited to handling systems with strong cross-coupling, and can be easily extended to include additional controlled variables and actuators. As scenarios that exhibit stronger coupling are explored, or as additional actuators and controlled outputs are considered, the tuning of separate PID loops will become more difficult, while the MIMO control design approach will still be appropriate.

5. Conclusion

A novel approach to controlling q_0 and β_N in NSTX-U, in which the outer-midplane wall gap and total beam power serve as manipulated variables, has been proposed. TRANSP simulations of the control schemes show promising results and motivate future experimental implementation. In future work, manipulation of the outer-gap will be integrated into a more complex current profile control scheme that includes modulation of the individual beam powers, plasma density, and loop voltage, to control several points of the safety factor profile simultaneously. The effect of the control scheme on plasma stability and controllability will also be studied in future research, as modifying the outer gap will vary coupling to the passive plates.

As part of this work, a flexible framework for performing feedback control design and simulation in the TRANSP has been developed. This framework will aid in the creation of advanced control algorithms by providing a means for conducting system identification simulations and high-fidelity tests of

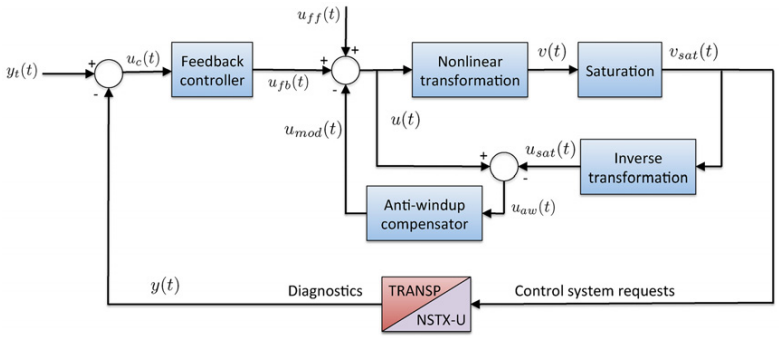

Figure A1. Schematic of control algorithm implementation.

proposed algorithms prior to experimental implementation and testing. In future work, the framework will be extended to include additional actuators and 'measurements' in order to test many of the advanced control algorithms under development for NSTX-U, including plasma boundary shape controllers and profile (safety factor, rotation, etc.) controllers. The framework is also planned to be used for studies of other machines, including DIII-D, ITER, and FNSF (Fusion Nuclear Science Facility).

Acknowledgments

This research was supported in part by an appointment to the U.S. Department of Energy Fusion Energy Postdoctoral Research Program administered by the Oak Ridge Institute for Science and Education and by the US Department of Energy Grant under Contract No. DE-AC02-09CH11466.

Appendix A. Controller algorithm implementation details

A schematic of the control algorithm implemented in the Expert routine is given in figure A1. The feedback control signal is calculated as the output of the system

$$x_{c,k+1} = A_c x_{c,k} + B_c u_{c,k},$$
$$y_c^k = C_c x_{c,k} + D_c u_{c,k}, \tag{A.1}$$

where A_c, B_c, C_c, and D_c are the user-specified controller system matrices, x_c is the controller state, u_c is the input to the controller, and y_c is the output of the controller. The vector u_c is composed of the error measurements

$$u_c = y_{\text{tar}} - y, \tag{A.2}$$

where y is the measured output, y_{mod} is the output modification signal from the anti-windup calculation (to be described) and y_{tar} is the corresponding set of targets. The vector y_c represents the feedback portion of the actuator requests, u, i.e.

$$u_{\text{fb}} = y_c, \tag{A.3}$$
$$u_{\text{ff}} = u_r + u_{\text{FFC}} \tag{A.4}$$
$$u = u_{\text{ff}} + u_{\text{fb}} + y_{\text{aw}}. \tag{A.5}$$

The term u_{mod} is the actuator modification signal from the anti-windup calculation. The feedforward term u_{ff} is the combination of a user-specified set of actuator trajectories determined offline and the result of calculations of an online feedforward compensator (to be used, for example, to account for measurable disturbances). A nonlinear transformation of the request u is applied to calculate the physical actuator requests v, i.e.

$$v = f(u). \tag{A.6}$$

The default transformation is simply $v = u$, however, alternative transformations can be used to allow greater control design flexibility (such a transformation is used in section 4.2). We consider the presence of saturation limits on the actuators, and calculate

$$v_{\text{sat}} = \text{sat}(v), \tag{A.7}$$
$$u_{\text{sat}} = f^{-1}(v_{\text{sat}}), \tag{A.8}$$

where v_{sat} is the final actuator request, and we have applied the inverse of the transformation (A.6) to calculate the saturated controller request u_{sat}. The anti-windup signal, used to keep the closed loop system well behaved in the presence of actuator saturation, is calculated as the output of the system

$$x_{\text{aw,k+1}} = A_{\text{aw}} x_{\text{aw,k}} + B_{\text{aw}} u_{\text{aw,k}},$$
$$y_{\text{aw,k}} = C_{\text{aw}} x_{\text{aw,k}} + D_{\text{aw}} u_{\text{aw,k}}, \tag{A.9}$$

where A_{aw}, B_{aw}, C_{aw}, and D_{aw} are the system matrices, x_{aw} is the state of the anti-windup system, and

$$u_{\text{aw}} = u - u_{\text{sat}}, \tag{A.10}$$

At the start of each transport time step in TRANSP (the shortest time scale in the simulation), the time since the last control calculation is compared with the desired controller sample time, T, to determine whether a control update should take place. Because the beam and geometry calculations are performed with longer step sizes than the transport calculations, and the inputs to these calculations cannot be updated at arbitrary times, control updates are aligned such that they take place just before the intervals at which these quantities are normally read in by TRANSP and the beam/geometry calculation step size is chosen to be a multiple of the controller sample time. The calculated actuator requests are saved and remain fixed until the next controller update, i.e. through several beam/geometry steps.

References

[1] Menard J. *et al* 2012 *Nucl. Fusion* **52** 083015
[2] Ono M. *et al* 2000 *Nucl. Fusion* **40** 557

[3] Sykes A. *et al* 2001 *Nucl. Fusion* **41** 1423
[4] Goldston R.J. *et al* 2008 An experiment to tame the plasma material interface *Proc. 22nd Int. Conf. on Fusion Energy (Geneva, Switzerland, 2008)* (Vienna: IAEA) FT/P3-12 www-naweb.iaea.org/napc/physics/FEC/FEC2008/html
[5] Stambaugh R.D. *et al* 2010 Candidates for a fusion nuclear science facility (FDF and ST-CTF) *37th EPS Conf. on Plasma Physics (Dublin, Ireland)* vol 51 P2.110 http://ocs.ciemat.es/EPS2010PAP/pdf/P2.110.pdf
[6] Menard J. *et al* 2011 *Nucl. Fusion* **51** 103014
[7] Kaye S. *et al* 2006 *Nucl. Fusion* **46** 848
[8] Kaye S. *et al* 2007 *Phys. Rev. Lett.* **98** 175002
[9] Kaye S. *et al* 2007 *Nucl. Fusion* **47** 499
[10] Valovic M. *et al* 2011 *Nucl. Fusion* **51** 073045
[11] Fredrickson E.D. *et al* 2006 *Phys. Plasmas* **13** 056109
[12] Gryaznevich M. *et al* 2008 *Nucl. Fusion* **48** 084003
[13] Podesta M. *et al* 2009 *Phys. Plasmas* **16** 056104
[14] Fredrickson E.D. *et al* 2009 *Phys. Plasmas* **16** 122505
[15] Gates D. *et al* 2007 *Nucl. Fusion* **47** 1376
[16] Menard J. *et al* 2007 *Nucl. Fusion* **47** S645
[17] Gates D. *et al* 2009 *Nucl. Fusion* **49** 104016
[18] Gerhardt S. *et al* 2011 *Nucl. Fusion* **51** 073031
[19] Buttery R. *et al* 2004 *Nucl. Fusion* **44** 1027
[20] Chapman I. *et al* 2011 *Nucl. Fusion* **51** 073040
[21] Erickson K. *et al* 2014 *Fusion Eng. Des.* **89** 853
[22] Gates D. *et al* 2006 *Nucl. Fusion* **46** 17
[23] Gerhardt S. *et al* 2010 *Fusion Sci. Technol.* **61** 11
[24] Kolemen E. *et al* 2010 *Nucl. Fusion* **50** 105010
[25] Kolemen E. *et al* 2011 *Nucl. Fusion* **51** 113024
[26] Kolemen E. *et al* 2013 *Fusion Eng. Des.* **88** 2757
[27] Levinton F.M. and Yuh H. 2008 *Rev. Sci. Instrum.* **79** 10F522
[28] Ferron J. *et al* 1998 *Nucl. Fusion* **38** 1055
[29] Ou Y. *et al* 2007 *Fusion Eng. Des.* **82** 1153
[30] Barton J.E. *et al* 2012 *Nucl. Fusion* **52** 123018
[31] Boyer M.D. *et al* 2013 *Plasma Phys. Control. Fusion* **55** 105007
[32] Boyer M.D. *et al* 2014 *IEEE Trans. Control Syst. Technol.* **22** 1725
[33] Moreau D. *et al* 2008 *Nucl. Fusion* **48** 106001
[34] Moreau D. *et al* 2011 *Nucl. Fusion* **51** 063009
[35] Turnbull A.D., Lin-Liu Y.R., Miller R.L., Taylor T.S. and Todd T.N. 1999 *Phys. Plasmas* **6** 1113
[36] Holcomb C.T. *et al* 2009 *Phys. Plasmas* **16** 056116
[37] Gerhardt S., Andre R. and Menard J. 2012 *Nucl. Fusion* **52** 083020
[38] Menard J. *et al* 2005 *Nucl. Fusion* **45** 539
[39] Menard J. *et al* 2006 *Phys. Rev. Lett.* **97** 095002
[40] Chapman I. *et al* 2010 *Nucl. Fusion* **50** 045007
[41] Breslau J. *et al* 2011 *Nucl. Fusion* **51** 063027
[42] Gerhardt S. *et al* 2009 *Nucl. Fusion* **49** 032003
[43] Hawryluk R. 1981 An empirical approach to tokamak transport *Physics of Plasmas Close to Thermonuclear Conditions* ed B. Coppi *Proc. Course Held in Varenna, Italy (Varenna, Italy, 27 August–8 September 1979)* vol 1, pp 19–46 (Amsterdam: Elsevier) http://w3.pppl.gov/transp/papers/Hawryluk.pdf
[44] Budny R. 1994 *Nucl. Fusion* **34** 1247
[45] TRANSP Homepage 2014 http://w3.pppl.gov/transp/
[46] Pankin A., Mccune D., Andre R., Bateman G. and Kritz A. 2004 *Comput. Phys. Commun.* **159** 157
[47] Huang J. and Menard J. 2005 Development of an auto-convergent free-boundary axisymmetric equilibrium solver *47th Annual DPP Meeting (Denver, CO, 2005)* www.osti.gov/scitech/servlets/purl/1051805
[48] Andre R. 2012 TRANSP/PTRANSP isolver free boundary equilibrium solver *54th Annual DPP Meeting (Providence, RI, 2012)* http://meeting.aps.org/Meeting/DPP12/Session/JP8.123
[49] Tala T. *et al* 2005 *Nucl. Fusion* **45** 1027
[50] Kim S.H. *et al* 2009 *Plasma Phys. Control. Fusion* **51** 105007
[51] Barton J.E., Besseghir K., Lister J. and Schuster E. 2013 *52nd IEEE Conf. on Decision and Control (Firenze, Italy)* p 4194 http://ieeexplore.ieee.org/xpls/abs_all.jsp?arnumber=6760533&tag=1
[52] Barton J.E. *et al* 2013 *52nd IEEE Conf. on Decision and Control (Firenze, Italy)* p 4182 http://ieeexplore.ieee.org/xpl/abstractAuthors.jsp?arnumber=6760531
[53] Zarnstorff M.C. *et al* 1990 *Phys. Fluids* B **2** 1852
[54] Sauter O., Angioni C. and Lin-Liu Y.R. 1999 *Phys. Plasmas* **6** 2834
[55] Lin-Liu Y.R. and Hinton F.L. 1997 *Phys. Plasmas* **4** 4179
[56] Staebler G., Colyer G., Kaye S., Kinsey J. and Waltz R. 2008 Testing the trapped gyro-landau fluid transport model with data from tokamaks and spherical Tori *Proc. 22nd IAEA Fusion Energy Conf. (Geneva, Switzerland, 2008)* (Vienna: IAEA) TH/P8-43 www-naweb.iaea.org/napc/physics/FEC/FEC2008/html/index.htm
[57] Chang C.S. 1982 *Phys. Fluids* **25** 1493
[58] Greenwald M. *et al* 1988 *Nucl. Fusion* **28** 2199
[59] Greenwald M. 2002 *Nucl. Fusion* **44** R27
[60] ITER Physics Experts Groups 1999 *Confinement and Transport and Confinement Modelling and Database* ITER Physics Basis Editors *Nucl. Fusion* **39** 2175
[61] Ljung L. 1999 *System Identification: Theory for the User* 2nd edn (Upper Saddle River, NJ: Prentice Hall)
[62] MATLAB and System Identification Toolbox Release 2013a
[63] Franklin G., Powell J. and Workman M. 1990 *Digital Control of Dynamic Systems* 2nd edn (Reading, MA: Addison-Wesley)
[64] Aström K. and Murray R. 2010 *Feedback Systems: An Introduction for Scientists and Engineers* (Princeton, NJ: Princeton University)
[65] Ramakrishnan S. *et al* 2011 Power system for NSTX upgrade *Technical Report* (*Princeton Plasma Physics Laboratory, Princeton, NJ*) http://ieeexplore.ieee.org/xpls/abs_all.jsp?arnumber=6052347&tag=1
[66] Xue D., Chen Y. and Atherton D. 2008 *Linear Feedback Control: Analysis and Design with MATLAB (Advances in Design and Control)* (Philadelphia, PA: Society for Industrial and Applied Mathematics)